Macromolecules

Article

pubs.acs.org/Macromolecules

Structuring of Thin-Film Polymer Mixtures upon Solvent Evaporation

C. Schaefer,[*,†,∥] J. J. Michels,[‡,⊥] and P. van der Schoot[§,∥]

[†]Dutch Polymer Institute, P.O. Box 902, 5600 AX Eindhoven, The Netherlands

[‡]Holst Centre/TNO, High Tech Campus 31, 5656 AE Eindhoven, The Netherlands

[§]Institute for Theoretical Physics, Utrecht University, Leuvenlaan 4, 3584 CE Utrecht, The Netherlands

[∥]Theory of Polymers and Soft Matter, Eindhoven University of Technology, P.O. Box 513, 5600 MB Eindhoven, The Netherlands

[⊥]Max Planck Institute für Polymerforschung, Ackermannweg 10, 55128 Mainz, Germany

ABSTRACT: We theoretically study the impact of solvent evaporation on the dynamics of isothermal phase separation of ternary polymer solutions in thin films. In the early stages we obtain a spinodal length scale that decreases with time under the influence of ongoing evaporation. After that rapid demixing occurs at a well-defined lag time, a morphology emerges of which the compositions of the coexisting phases rapidly approach the binodal values. We find that the type of morphology, which can be either bicontinuous or dispersed, strongly depends on the evaporation rate if the solubility of the two solutes in the common solvent differs. We derive expressions that relate both the lag time and length scale characterizing the emerging morphology to all relevant physical parameters. These include the tracer diffusivities, the interaction parameters, the degrees of polymerization, the blend composition, and the evaporation rate. In agreement with our numerical results, we find the latter to scale with a one-sixth power of the evaporation rate. Following the lag time, a new length scale appears that increases with time due to coarsening. If evaporation is sufficiently slow, this length increases with the conventional one-third power of time. For rapid evaporation deviations from that may occur, especially if the solvent compatibility of the solutes differ. Our model calculations suggest that the characteristic features of the final dry-film morphology is dictated by the quench depth as well as the time available for coarsening, which are both determined by the rate of evaporation.

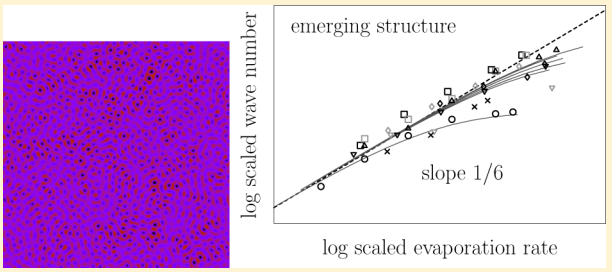

INTRODUCTION

State-of-the-art organic and hybrid thin-film electronic devices usually contain at least one layer based on a blend of polymeric or small molecular species, whose individual electronic properties cooperatively give rise to a specific functionality.[1−4] Such blend films have a thickness of the order of a hundred nanometers and are typically deposited via solution casting, e.g., spin coating, under evaporative conditions. Optimal device performance often requires the blend components to phase separate. Examples of such devices include organic solar cells,[1−4] organic memory diodes,[5−8] and transistors.[9,10] Moreover, outside of organic electronics thin-film polymer blends are relevant to membrane technology,[11−13] nanoporous implants for controlled drug delivery,[14] and scaffolds for tissue engineering.[15]

A frequently observed mode of phase separation, notably observed for ferroelectric diodes[5−8] and organic solar cells,[16,17] is solution-stage spinodal decomposition and coarsening. During this process, the blend components spontaneously demix once solvent evaporation has caused the composition to be pushed from the single-phase region into the unstable part of the miscibility gap of the ternary phase diagram. This isothermal destabilization by solvent evaporation has been loosely dubbed a "solvent quench" in order to set it apart from the more usual temperature quench. In both, demixing as well as coarsening principally determines the predominant length scale of structural features in the phase-separated morphology. However, in solvent quenching ongoing evaporation causes the viscosity to increase up to the point where mass transport arrests, essentially "freezing" the morphology in the dry film.

Several experimental studies have shown faster evaporation to lead to smaller features in the dry-layer morphology.[16−21] However, the question whether, or under what conditions, early stage demixing or late-stage coarsening dominates the determination of these feature sizes has so far been left unanswered. This is somewhat surprising, as it is well-known that the device performance strongly depends on the morphology. Note also that we cannot rely on what is known about structure development in temperature-quenched systems, which has been studied extensively over the past 50 odd years. What is missing is the development of theory that addresses the coupling between evaporation and structure development in chemically complex mixtures. That this must be the case, we deduce from a number of theoretical studies considering a time-dependent overall composition, e.g., due to reversible chemical

Received: March 16, 2016
Revised: July 11, 2016
Published: September 2, 2016

DOI: 10.1021/acs.macromol.6b00537
Macromolecules 2016, 49, 6858−6870

conversion,[22,23] polymerization,[24] or evaporation from a single-polymer solution.[25]

In this work, we account for this deficit by presenting a theoretical study that identifies how evaporation significantly alters the dynamics of both early stage demixing and late-stage coarsening in solvent-borne polymer blends. We perform numerical as well as approximate analytical calculations focusing on diffusive dynamics, specifically aiming at comparing blends relevant to organic photovoltaics to idealized model systems. As we shall see, evaporation causes the spinodal length scale to become time dependent and after a lag time to lead to rapid demixing into domains with solute concentrations that are virtually identical to those in equilibrium. However, because evaporation is ongoing, these concentrations evolve as a function of time. This affects the coarsening kinetics, in particular if the mixture is off-critical. It turns out that the lag time and associated predominant length scale can be predicted as a function of all relevant physical parameters, such as the molecular weight of the solutes and their solubilities in the common solvent. Finally, we compare our calculations with the experimentally observed evaporation-rate dependence of the predominant length scale of the dry-film morphologies of photoactive layers in organic solar cells.

The remainder of this article is arranged as follows. We first present a two-dimensional generalized diffusion equation that includes solvent evaporation and discuss under what conditions the assumption of a quasi-two-dimensional model is valid. Subsequently, we provide input-parameter sets describing six different mixtures. Three of these find application in organic photovoltaics and are characterized with a difference in solubility of the two solutes in the solvent. The other three are idealized model mixtures, for which we set the solubility of both solutes equal for comparison. We present ternary phase diagrams for all six and for one discuss results of dynamical calculations by way of example. Next, we show that the early stage dynamics is in some sense universal and hence covers all six of our mixtures. In the late stages this seems also to be true albeit only if evaporation is sufficiently slow. In that case, the structure of the phase-separated mixture remains unaltered, that is, dispersed droplets of one phase in the other or bicontinuous. Coarsening then follows the prediction of classical theory. Deviation from classical theory may occur if evaporation is not slow. Droplets that form under slow evaporation need not form under conditions of fast evaporation, where instead initially a bicontinuous structure may emerge that later on breaks up into droplets. We end our paper with a discussion and conclusions. In our discussion we compare our findings with experimental dry-layer morphologies and their dependence on the evaporation rate. We argue that these must be predominantly determined by the late-stage coarsening in the slow-evaporation limit.

GENERALIZED DIFFUSION MODEL WITH EVAPORATION

To investigate evaporation-induced phase separation, we make use of coupled generalized diffusion equations for a ternary polymer solution, i.e., two polymers that we denote A and B in a solvent S. We include a prescription for steady solvent evaporation, which increases the concentration of the solutes and hence their interaction that in our model drives phase separation of the unlike solutes. Solvent evaporation is on the one hand fast enough for nucleation not to play a role when traversing the metastable regime between the binodal and spinodal branches,[26] and hence that phase separation takes place via spinodal decomposition. On the other hand, it is also slow enough so that stratification does not play a role and a quasi-two-dimensional description suffices.[25,27−29] This description is valid under conditions of weak interface adsorption and fast diffusion that counteracts the accumulation of material near the surface due to evaporation. The latter applies if the Biot numbers for the two solutes are much smaller than unity.[a,28,29]

If our solution were compressible, the continuity equations dictate that the time evolution of the volume fraction $\phi_m(\mathbf{r},t)$ of component m = A, B, S at position $\mathbf{r}$ in our two-dimensional domain at time t obeys

$$\partial_t \phi_m + \nabla\cdot\mathbf{j}_m = \sigma_m + \zeta_m \tag{1}$$

Here, $\mathbf{j}_m(\mathbf{r},t)$ is the mass current of component m. On the right-hand side of eq 1 we have added a source term σ_m that accounts for evaporation and a noise term ζ_m that describes thermally induced density fluctuations. In the following, we will describe the various ingredients point by point starting with the contribution of the mass currents.

Within linear nonequilibrium thermodynamics, diffusive mass transport is driven by gradients in all of the chemical potentials μ_A, μ_B, and μ_S of the two solutes and the solvent[30]

$$\mathbf{j}_m = -\sum_n L_{mn}\nabla\mu_n \tag{2}$$

where $L_{mn} = L_{nm}$ denotes the symmetric Onsager mobility coefficients for m, n = A, B, and S. As usual,[31,32] the solution is treated as incompressible, and the volume fractions add up to unity: $\phi_A + \phi_B + \phi_S = 1$. This means that the mass currents of the three components are no longer independent, and this has consequences on the one hand for the chemical potentials and on the other hand for the mobilities. Let us first deal with the chemical potentials.

Chemical potentials can be calculated from a free energy functional, which we write as

$$\mathcal{F}[\phi_A, \phi_B] = \int \mathrm{d}\mathbf{r}[f_{\mathrm{loc}}(\phi_A, \phi_B) + f_{\text{non-loc}}(\phi_A, \phi_B)] \tag{3}$$

which is a spatial integral over a dimensionless local free energy density, f_{loc}, and a dimensionless nonlocal free energy density, $f_{\text{non-loc}}$. Here, we have already presumed incompressibility; that is, we have removed an explicit dependence of the free energy densities on ϕ_S, which depend only on ϕ_A and ϕ_B. Furthermore, in eq 3 and below we express free energies in units of thermal energy k_BT, with k_B Boltzmann's constant and T the temperature, and the position in space $\mathbf{r}$ in units of the size of an elementary molecular building block, presumed equal for both polymers A and B as well as for the solvent, S.

For the local contribution, we invoke the dimensionless Flory−Huggins free energy density[33−35]

$$\begin{aligned} f_{\mathrm{loc}} = {} & \frac{1}{N_A}\phi_A \ln\phi_A + \frac{1}{N_B}\phi_B \ln\phi_B + (1-\phi_A-\phi_B) \\ & \times \ln(1-\phi_A-\phi_B) + \phi_A\phi_B\chi_{AB} + (1-\phi_A-\phi_B) \\ & \times [\phi_A\chi_{AS} + \phi_B\chi_{BS}] \end{aligned} \tag{4}$$

where χ_{AB}, χ_{AS}, and χ_{BS} are the usual Flory−Huggins interaction parameters and N_A and N_B are the degrees of polymerization of the two solutes. The size of the solvent, N_S, is set to unity.

The nonlocal contribution to the free energy penalizes concentration gradients. It gives rise to the spinodal length scale

DOI: 10.1021/acs.macromol.6b00537
Macromolecules 2016, 49, 6858−6870

and the interfacial tension that ultimately drives coarsening. Within a square-gradient theory for an incompressible three-component system, we have

$$f_{\text{non-loc}} = \frac{1}{2}\kappa_{AA}\left|\nabla\phi_A\right|^2 + \frac{1}{2}\kappa_{BB}\left|\nabla\phi_B\right|^2 + \kappa_{AB}\nabla\phi_A < \nabla\phi_B \tag{5}$$

where the κs are "stiffness" coefficients.[36] In principle, these coefficients consist of contributions from a reduction of the polymer-chain conformational entropy in concentration gradients as well as from the interactions between the molecular units.[31,37−40] For reasons of simplicity, we take the stiffnesses as free parameters that are subject to the condition $2\kappa_{AB} < \kappa_{AA} + \kappa_{BB}$. This guarantees that concentration gradients are always penalized.

Returning to the chemical potentials, these can be obtained from the free energy by performing functional derivatives with respect to the various densities. However, due to the incompressibility approximation our free energy in eq 3 does not allow us to do that directly. Indeed, it allows us to only calculate *exchange* chemical potentials by taking the functional derivatives of the free energy

$$\Delta\mu_A \equiv \frac{\delta\mathcal{F}}{\delta\phi_A} = \frac{\partial f_{\text{loc}}}{\partial\phi_A} - \kappa_{AA}\nabla^2\phi_A - \kappa_{AB}\nabla^2\phi_B \tag{6}$$

and by

$$\Delta\mu_B \equiv \frac{\delta\mathcal{F}}{\delta\phi_B} = \frac{\partial f_{\text{loc}}}{\partial\phi_B} - \kappa_{AB}\nabla^2\phi_A - \kappa_{BB}\nabla^2\phi_B \tag{7}$$

These are related to the earlier introduced ones by $\Delta\mu_A = \mu_A - \mu_S$ and $\Delta\mu_B = \mu_B - \mu_S$ and describe the change in the free energy density due to the replacement of solvent by components A or B.

In order to express the mass currents in eq 2 as a function of the exchange chemical potentials rather than the usual ones, we express the chemical potentials of components A, B, and S in terms of the exchange chemical potentials of components A and B. We do this by writing $\mu_A = \Delta\mu_A + \mu_S$, $\mu_B = \Delta\mu_B + \mu_S$, and $\mu_S = \mu_S$. By making use of the Gibbs−Duhem relation, $\phi_A\nabla\mu_A + \phi_B\nabla\mu_B + \phi_S\nabla\mu_S = 0$, we can relate μ_S to the exchange chemical potentials of components A and B. We find from straightforward algebra and making explicit use of incompressibility, i.e., demanding that the various volume fractions add up to unity.

$$\nabla\mu_S = -\phi_A\nabla\Delta\mu_A - \phi_B\nabla\Delta\mu_B \tag{8}$$

Hence, the gradient in bare chemical potential of solute A is given by

$$\nabla\mu_A = (1-\phi_A)\nabla\Delta\mu_A - \phi_B\nabla\Delta\mu_B \tag{9}$$

and that of solute B is given by

$$\nabla\mu_B = -\phi_A\nabla\Delta\mu_A + (1-\phi_B)\nabla\Delta\mu_B \tag{10}$$

Now that we have worked around the chemical potentials in incompressible systems, we need to address how incompressibility affects the Onsager coefficients, L_{mn}, turning them into a smaller number of effective ones. First we note that the diagonal elements of the mobility matrix, L_{mm}, are related to the tracer diffusivities by $L_{mm}(\mathbf{r},t) = \phi_m(\mathbf{r},t)\,N_m + D_m$ because under conditions where component m is dilute mass transport should obey Fickian diffusion, $\mathbf{j}_m = -D_m\nabla\phi_m$. Note that, as advertised, $N_S \equiv 1$, and D_m is a tracer diffusivity that in principle depends on the composition of the mixture.[31] The off-diagonal elements, which are symmetric on account of the Onsager reciprocity relations, can (in principle) be related to microscopic velocity−velocity correlation functions through the Green−Kubo relations.[41] However, since these cross-correlations are typically not known in complex mixtures, we only take the diagonal elements into account, $\Lambda_m \equiv L_{mm}$, by ignoring the cross-mobilities in the Onsager relations, $L_{n,m\neq n}$. The mass currents of different solutes remain coupled through the incompressibility assumption, $\sum_m \mathbf{j}_m = \mathbf{0}$.[30]

The incompressibility assumption suppresses inhomogeneities in the density and is enforced either by introducing advective mass transport in the so-called *fast-mode theory*[32] or by applying the so-called *slow-mode theory*. In slow-mode theory an effective potential U is added to the chemical potential of the solutes that enforces that the sum of currents add up to zero.[31] For mixtures in which all components, including the solvent, have the same molecular volume and the same diffusivity, fast- and slow-mode theory are equal.[31,32] However, if one component is much more mobile than the others, fast-mode theory predicts that this component dominates the kinetics, whereas in slow-mode theory this is true for the slowest components. From calculations that we do not present in this work, we conclude that our key findings do not depend on the choice between fast- and slow-mode mobilities.

Focusing our discussion on slow-mode theory, the transport equations can be written as[31,42]

$$\mathbf{j}_m = -\Lambda_m\nabla(\mu_m + U) \quad \text{for } m = \text{A, B, S} \tag{11}$$

with Λ_m the diagonal components of the Onsager mobilities. From the incompressibility relation $\sum_m \mathbf{j}_m = \mathbf{0}$ we conclude that the effective potential, U, obeys $\nabla U = -(\Lambda_A\nabla\mu_A + \Lambda_B\nabla\mu_B + \Lambda_S\nabla\mu_S)/(\Lambda_A + \Lambda_B + \Lambda_S)$.[31] If we insert this into the transport equations of eq 11, and substitute the chemical potential gradient, $\nabla\mu_m$, by the exchange chemical potential $\nabla\Delta\mu_m = \nabla\mu_m - \nabla\mu_S$ from with the gradients in bare chemical potential given in eqs 8−10, we obtain

$$\mathbf{j}_A = -\Lambda_{AA}\nabla\Delta\mu_A - \Lambda_{AB}\nabla\Delta\mu_B \tag{12}$$

and

$$\mathbf{j}_B = -\Lambda_{BA}\nabla\Delta\mu_A - \Lambda_{BB}\nabla\Delta\mu_B \tag{13}$$

Here, we have introduced the slow-mode mobility coefficients

$$\Lambda_{AA} = \frac{\Lambda_A(\Lambda_B + \Lambda_S)}{\Lambda_A + \Lambda_B + \Lambda_S} \tag{14}$$

$$\Lambda_{AB} = \Lambda_{BA} = -\frac{\Lambda_A\Lambda_B}{\Lambda_A + \Lambda_B + \Lambda_S} \tag{15}$$

and

$$\Lambda_{BB} = \frac{\Lambda_B(\Lambda_A + \Lambda_S)}{\Lambda_A + \Lambda_B + \Lambda_S} \tag{16}$$

In case the layer is dry, if $\phi_S = 0$, we retrieve from these expressions those for the classical incompressible binary mixture of components A and B, $\mathbf{j}_A = -\mathbf{j}_B = -\Lambda_{AA}\nabla(\mu_A - \mu_B)$ with $\Lambda_{AA} = \Lambda_{BB} = -\Lambda_{AB}$. In the other extreme case where $\Lambda_S \gg \Lambda_A, \Lambda_B$, we find that the mobilities in eqs 14−16 reduce to $\Lambda_{AA} \approx \Lambda_A$, $\Lambda_{BB} \approx \Lambda_B$, and $\Lambda_{AB} \approx 0$. Hence, the fastest mode

DOI: 10.1021/acs.macromol.6b00537
Macromolecules 2016, 49, 6858−6870

drops out, and the kinetics are determined by the slowest components.

Finally, to obtain the generalized diffusion equations, we insert our mass currents, which now enforce incompressibility, into the continuity equations (1), giving

$$\frac{\partial \phi_A}{\partial t} = \nabla\cdot\Lambda_{AA}\nabla\Delta\mu_A + \nabla\cdot\Lambda_{AB}\nabla\Delta\mu_B + \sigma_A + \zeta_A \tag{17}$$

for component A and

$$\frac{\partial \phi_B}{\partial t} = \nabla\cdot\Lambda_{BA}\nabla\Delta\mu_A + \nabla\cdot\Lambda_{BB}\nabla\Delta\mu_B + \sigma_B + \zeta_B \tag{18}$$

for component B.

This leaves us to discuss the evaporation terms, σ_A and σ_B, and the noise terms, ζ_A and ζ_B, in these equations. Starting with the first, presuming that only the solvent evaporates, the overall solute concentration $\phi \equiv \phi_A + \phi_B$ increases in time due to evaporation. This happens at a rate $\alpha(\mathbf{r},t) \equiv \partial\phi(\mathbf{r},t)/\partial t$ that in principle depends on the local composition, vapor pressure, time, and so on.[43] To simplify interpretation of our findings and control the evaporation rate, we ignore any local and temporal variations. In that case α becomes a control variable.[b] This then translates to the evaporation terms in eqs 17 and 18 as $\sigma_A = \alpha\phi_A/(\phi_A + \phi_B)$ and $\sigma_B = \alpha\phi_B/(\phi_A + \phi_B)$.

We need to supplement our kinetic equations with initial conditions. As already advertised, we ignore nucleation processes for the short time needed to traverse the metastable region in the phase diagram. Hence, in our calculations phase separation starts when the solution crosses the spinodal concentration, $\phi_0 = \phi_A(\mathbf{r}, t = 0) + \phi_B(\mathbf{r}, t = 0)$. At that point we know the overall composition of the solution because it is fixed. The spinodal we calculate by evaluating the determinant of the Hessian of our local free energy in eq 4 and equating it to zero. This fixes $\phi_A(\mathbf{r}, t = 0)$ and $\phi_B(\mathbf{r}, t = 0)$ if we equate them to the uniform spinodal concentrations. Because of our assumption of steady evaporation, at time $t = (1 - \phi_0)/\alpha$ all the solvent has evaporated. This means that at time $t = (1 - \phi_0)/\alpha$ the layer is dry and that for longer times the kinetic equations of eqs 17 and 18 no longer apply. We stop the numerical evaluation at that point in time.

Finally, the stochastic noise terms obey the fluctuation–dissipation theorem, allowing us to connect them to our kinetic coefficients according to[44−48]

$$\langle\zeta_m(\mathbf{r}, t)\rangle = 0,$$
$$\langle\zeta_m(\mathbf{r}, t)\zeta_n(\mathbf{r}', t')\rangle = -2\nabla\Lambda_{mn}(\mathbf{r}, t)\nabla\delta(\mathbf{r} - \mathbf{r}')\delta(t - t') \tag{19}$$

for m, n = A, B. This now completes our discussion of all the ingredients of our theoretical description.

We numerically solve eqs 17 and 18 using a standard finite-difference method on a periodic 512 × 512 square lattice. We approximate gradients and curvatures using a central-difference description and perform time steps using adaptive explicit Euler steps.[49] Again, at $t = 0$ the mixture is homogeneous, and for $t > 0$ concentration fluctuations are implemented at each time step using the discretized form of eq 19. Details are given in the Appendix.

INPUT PARAMETERS AND NUMERICAL CALCULATIONS

The generalized diffusion equations of eqs 17 and 18 cannot be solved exactly for all times and conditions. Therefore, we rely in large part on a numerical evaluation. This we do for parameter values representing a variety of ternary solutions consisting of solutes A and B in a solvent S. Half of the mixtures we focus attention on find applications in organic photovoltaics,[16,17,27] and the remainder are idealized model mixtures for comparison. The mixtures for organic photovoltaics are asymmetric in the sense that the solutes A and B have different solubilities in the solvent S, whereas the model mixtures are symmetric in this sense. As we shall see below, whether or not the solution is symmetric has no impact on the early stage kinetics of phase separation but can affect the late stages.

The input-parameter sets corresponding to the various mixtures are presented in Table 1. Given are the Flory–Huggins interaction parameters, degrees of polymerization, gradient stiffnesses, diffusivities, and compositions. Entries I–III are the idealized mixtures, and entries IV–VI refer to the experimentally studied mixtures for which we take experimentally determined values for the various parameters.[16,17,27] The interaction parameters were established by means of contact-angle measurements, and the degrees of polymerization were estimated from the molecular weights.[16,17,27] According to our calculations, all mixtures have a single miscibility gap and under appropriate conditions show coexistence of two phases.

Table 1. Values of the Parameters for Mixtures of Solutes A and B in Solvent S[a]

mixture	χ_{AB}	χ_{AS}	χ_{BS}	N_A	N_B	D_B/D_A	A:B
I(a)	0.75	0.0	0.0	10	10	1	1:1
I(b)	0.75	0.0	0.0	10	10	1	1:2
II	0.75	0.0	0.0	100	100	1	1:2
III	1.5	0.0	0.0	10	10	1	1:2
IV(a)[16,17]	1.0	0.4	0.9	89	7	1	1:2
IV(b)[16,17]	1.0	0.4	0.9	89	7	10	1:2
V(a)[27]	1.1	0.36	0.9	720	5	10	1:1
V(b)[27]	1.1	0.36	0.9	720	5	10	1:4
VI[27]	0.45	0.51	0.89	66	5	10	1:4

[a]Mixtures I–III are symmetric, and mixtures IV–VI are asymmetric. The latter are applied for organic photovoltaic materials.[16,17,27] The χ's are dimensionless interaction parameters, the N's are the numbers of segments per molecule, the κ's are concentration-gradient stiffnesses, and the D's are tracer diffusivities. Further, the stiffnesses have values $\kappa_{AA} = \kappa_{BB} = 1$ and $\kappa_{AB} = 0.1$.

Mixture IV represents a "DPP" copolymer (diketopyrrolopyrrole–quinquethiophene) and a "$PC_{70}BM$" ([6,6]-phenyl-C_{71} -butyric acid methyl ester) fullerene derivative in the solvent chloroform.[16,17] Mixture V models a "F8" (poly(9,9-dioctylfluorenyl-2,7-diyl)) polymer and a "$PC_{60}BM$" ([6,6]-Phenyl C_{61}-butyric acid methyl ester) fullerene derivative in the solvent chlorobenzene.[27] Mixture VI is modeled on an "APFO-3" (poly[(9,9-dioctylfluorenyl-2,7-diyl)-*co*-5,5-(4′,7′-di-2-thienyl-2′,1′,3′-benzothiadiazole)]) polymer and a $PC_{60}BM$ fullerene derivative dissolved in chloroform.[27] Mixtures IV–VI have in common that the solubility of the polymer in the indicated solvents is larger than that of the fullerene derivatives. This expresses itself in solute–solvent interaction parameters which are nonzero and unequal degrees of polymerization. For the symmetric mixtures we put the solute–solvent interaction

DOI: 10.1021/acs.macromol.6b00537
Macromolecules 2016, 49, 6858−6870

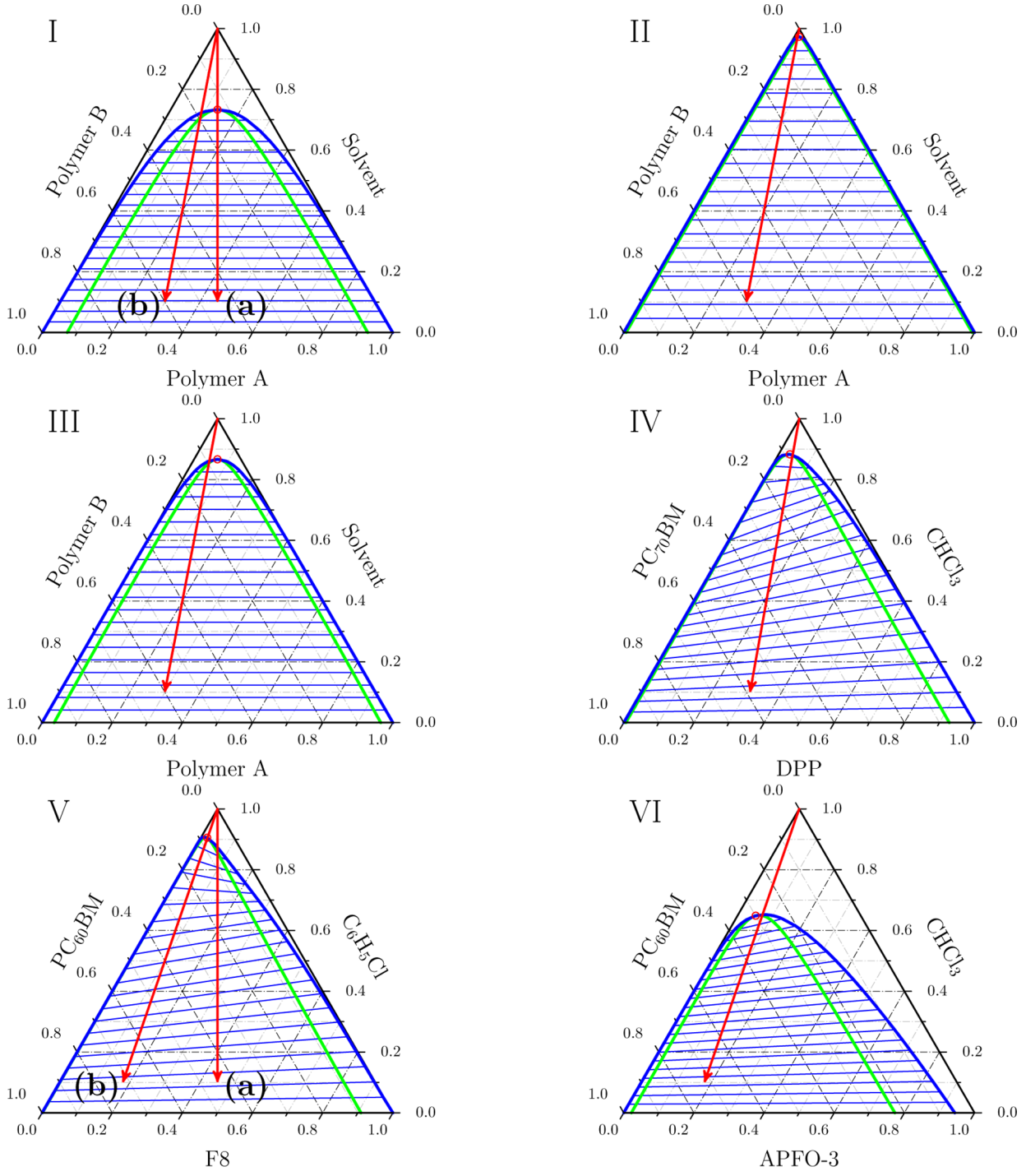

Figure 1. Calculated phase diagrams using the Flory–Huggins parameters of mixtures I–VI in Table 1. In blue (black) we have indicated the binodal of which the coexisting phases are connected by tie lines. The green (light gray) line represents the spinodal, and the red (dark gray) arrows represent the phase trajectories followed upon evaporation in our numerical simulations.

parameters equal to zero and choose equal degrees of polymerization. Mixtures I–III can be seen as pseudobinary blends where the effective repulsion between the solutes is reduced due to the presence of solvent.[50−53]

How this choice of parameters impacts upon the phase behavior of these different mixtures is shown in Figure 1. The phase diagrams in the figure we have calculated from Flory–Huggins theory.[c] Critical point, binodal, and spinodal are indicated in red (gray in print), blue (dark gray), and green (light gray), respectively. Tie lines connect phases at equal chemical potential and are indicated with thin blue (dark gray) lines.

As we can see from Figure 1, the phase diagrams of mixtures I–III are symmetric; that is to say, the critical point is located at a blend composition of value 0.5, and the tie lines are horizontal. This is not so for mixtures IV–VI. For mixtures IV and VI the tie lines have a positive slope, indicating that the polymer-rich phase is more dilute than the fullerene-rich phase. In other words, tilted tie lines indicate solvent partitioning takes place. For mixture V the sign of the slope depends on the

DOI: 10.1021/acs.macromol.6b00537
Macromolecules 2016, 49, 6858–6870

overall solvent content. For dilute solutions the sign of the slope is negative, implying that the polymer-rich phase is less pure than the fullerene-rich phase, whereas for concentrated ones the slope is positive.

To see how the evaporation rate impacts upon the phase separation, we take as a representative example mixture IV(b). The concentration path that we follow during the evaporation of solvent is indicated in Figure 1 by the red (dark gray) arrow as in fact for the other mixtures as well. In the process, the overall blend composition remains constant as only the solvent evaporates. To solve the dynamical equations, we need to input the tracer diffusivities of the various components. For the ratios of the tracer diffusivities of the solutes, we assume that they are equal to the ratio of their molecular size and is indicated in Table 1. The absolute time scale that we denote by τ_L in our numerical solution we present in the following section and is not of importance at this point.

Results of our numerical evaluation of the time evolution of phase separation induced by steady evaporation for the mixture IV(b) is given in Figure 2, for a very low dimensionless

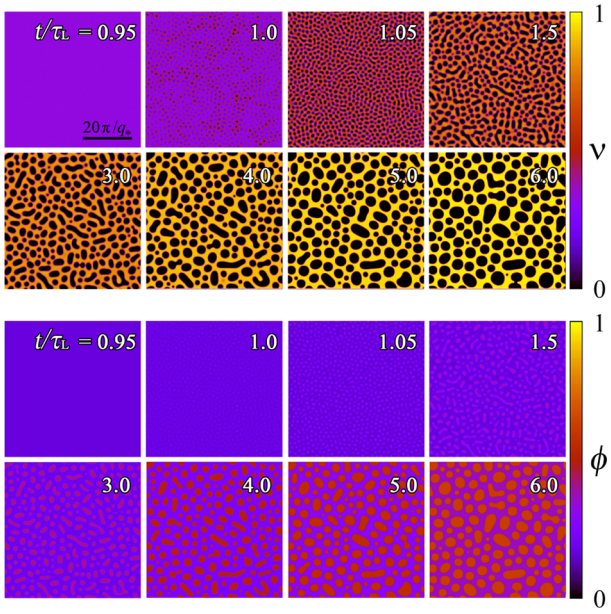

Figure 2. Evaporation-induced structure development in a ternary polymer solution. The color (grayscale) codings indicate differences in blend composition of the solute, $\nu = \phi_{DPP}/(\phi_{DPP} + \phi_{PC_{70}BM})$, and differences in total concentration $\phi = \phi_{DPP} + \phi_{PC_{70}BM}$, with ϕ_{DPP} and $\phi_{PC_{70}BM}$ the concentrations of DPP and $PC_{70}BM$ (fullerene), respectively. We have calculated these structures for the parameter values of mixture IV(b) in Table 1 and scaled evaporation $\tilde{\alpha} = 4 \times 10^{-7}$. The evaporation rate has been rendered dimensionless by the factor $1/\chi_{AB}\tau_L$ with χ_{AB} the interaction parameter between the solutes and τ_L is the lag time (see main text), defined by the time, t, at which a phase-separated structure becomes discernible (see also Figure 4).

evaporation rate of $\tilde{\alpha} = 4 \times 10^{-7}$ to be discussed in more detail in the following section. Indicated in the top series of images is the local composition, $\nu(\mathbf{r},t) = \phi_A(\mathbf{r},t)/\phi(\mathbf{r},t)$, and the bottom ones the local concentration, $\phi(\mathbf{r},t) = \phi_A(\mathbf{r},t) + \phi_B(\mathbf{r},t)$, as a function of dimensionless time. We recall that in our calculations the spinodal is traversed at time $t = 0$. Focusing on the top series, so the composition as a function of time, we find that for $t < \tau_L$ not much seems to be happening, while for $t > \tau_L$ a texture characterized by fullerene-rich droplets embedded in a polymer-rich matrix rapidly emerges and subsequently coarsens. Because of this, it seems natural to dub τ_L a "lag time" before phase separation seemingly sets off.[d] As we shall see, this is not quite accurate as spinodal decomposition does take place for $t < \tau_L$.

The bottom series in Figure 2, depicting the time evolution of the local total solute concentration, highlights the preference of the solvent for residing in the polymer-rich phase. This partitioning of solvent results from the difference in solubility of the two solutes. Because the polymer-rich phase is enriched in solvent, the more concentrated fullerene-rich phase becomes the dispersed phase despite its 2:1 excess. This is in agreement with experimental observations.[16]

If we increase the evaporation rate by a factor of 100, we obtain morphologies that are inverted as can be seen in Figure 3. In this case, first a bicontinuous structure emerges that

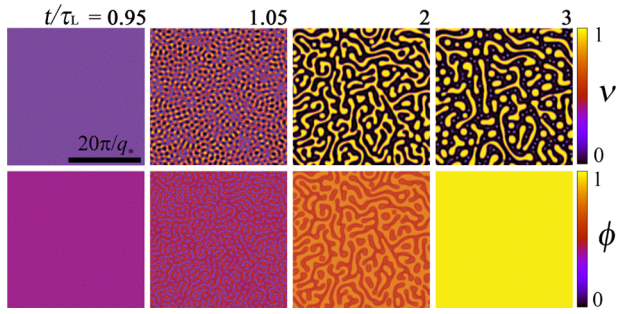

Figure 3. Evaporation-induced structure development in a ternary polymer solution. The color (grayscale) codings indicate differences in blend composition of the solute, $\nu = \phi_{DPP}/(\phi_{DPP} + \phi_{PC_{70}BM})$, and differences in total concentration $\phi = \phi_{DPP} + \phi_{PC_{70}BM}$, with ϕ_{DPP} and $\phi_{PC_{70}BM}$ the concentrations of DPP and $PC_{70}BM$ (fullerene), respectively. The parameters are equal to those in Figure 2, except that evaporation is 100 times faster.

subsequently breaks up into elongated polymer-rich droplets in a fullerene-rich phase. This is because for early times, where the solution is dilute, the two coexisting phases are equal in volume because the overall concentration and composition is close to the midpoint of the tie line. For later times, i.e., when the overall concentration is larger, the volume of the polymer-rich phase becomes smaller than that of the fullerene-rich phase because the overall concentration and composition are closer to the binodal of the fullerene-rich phase. Apparently, the evaporation rate in combination with the blend composition and the level of asymmetry of the phase diagram dictates what phase will be the dispersed phase and what phase will be the continuous phase.

From the images in Figures 2 and 3 more information can be extracted, e.g., the extent of phase separation and the typical length scale of the evolving structure (see Figure 4). The former we identify by probing the smallest and largest values of the blend composition ν in the entire domain. The latter we obtain from taking the Fourier transform of the local composition $\nu(\mathbf{r},t)$ (the structure factor). The green (light gray) symbols in Figure 4A represent the time evolution of the composition and confirm that with ongoing evaporation the composition variations remain small for times below τ_L. This is not surprising because the driving force for phase separation remains weak and the spinodal length scale, indicated with blue

DOI: 10.1021/acs.macromol.6b00537
Macromolecules 2016, 49, 6858−6870

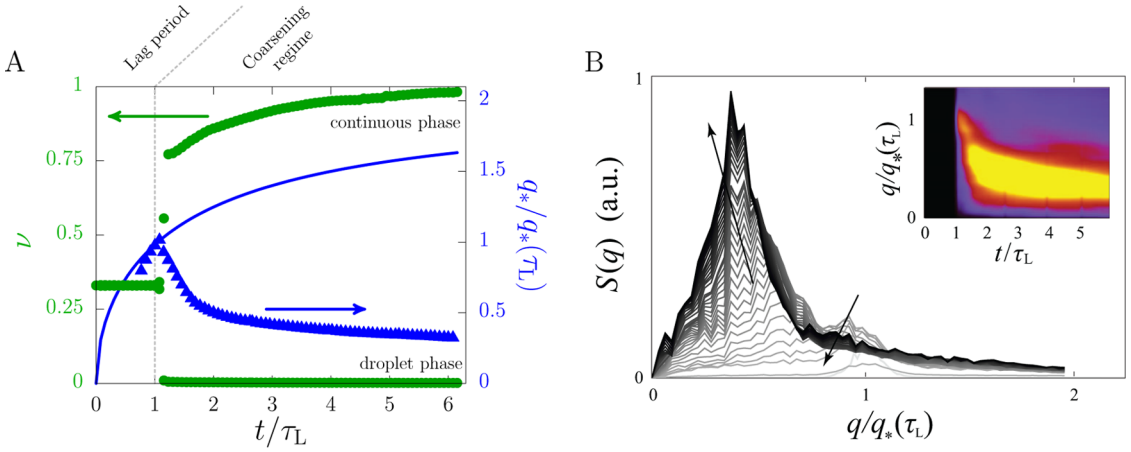

Figure 4. Structural development of the morphologies in Figure 2 as a function of time, t, in units of the lag time, τ_L. (A) The left axis indicates the composition in green (light gray), and the right axis indicates the wavenumber in blue (dark gray). The filled triangles represent the predominant structural wavenumber obtained numerically, whereas the solid line is predicted according to the linearized theory in eq 29 that is expected to hold for early times. (B) Structure factor, $S(q)$, for different times running from $t/\tau_L = 1$ (light gray) to $t/\tau_L = 5.0$ (black). The inset highlights the appearance of two structure peaks.

(dark gray) symbols, is large, requiring mass to be transported over large distances. As time proceeds, the mixture is further destabilized, and the spinodal length decreases until rapid bifurcation of the composition in the polymer-rich and polymer-poor regions takes place at time τ_L.

Shortly following the bifurcation, we find the composition and concentration of the coexisting phases to approach their respective binodal values. This means that the fullerene-rich phase is almost pure shortly after the lag time, whereas the polymer-rich phase initially contains a considerable amount of fullerene but becomes more pure as the overall concentration increases with time due to evaporation. Hence, the time evolution of the phase purity of the phase-separated domains is predominantly dictated by thermodynamics.

Now that we have discussed what phases that form in mixture IV(b) constitute the minority or majority phases, and what their phase purity is, we focus on the typical length scales. As already advertised, we probe these with the aid of the time-resolved static structure factor, $S(q)$, which we calculate by radially averaging the Fourier transform of the composition field. To perform the Fourier transform, we impose periodic boundary conditions. $q_*(t)$ in Figure 4A is the value of the momentum transfer at which the structure factor $S(q)$ takes its maximum value. For times $t < \tau_L$, we find it to increase with time because the solution moves increasingly deeply into biphasic regime due to evaporation.[24,25] Consequently, the mixture becomes increasingly unstable with time.

At time $t = \tau_L$, $q_*(\tau_L)$ takes its maximum value. It seems plausible that the associated length scale can be identified as an emerging structural wavenumber that potentially dictates the late-stage structure in the dry film. For times $t > \tau_L$, the structural length scale increases with time on account of coarsening. How much of the emerging structural length scale survives depends on how much time remains for coarsening to modify it. If there is sufficient time for the emerging structure to coarsen, information about it will be lost.

Figure 4A shows that the emerging structural length scale increases more rapidly for short times following the bifurcation than for later times, suggesting that different processes are at play. Inspection of the late-stage structure factor in Figure 4B confirms this. This figure shows that following the emergence of the spinodal peak at the wave vector $q_*(\tau_L)$, a second peak appears at a smaller wavenumber. The spinodal peak decreases in intensity, whereas the peak height associated with the second length increases with time. The two time scales mentioned correlate with these two processes. The question now arises as to what causes the second length scale to appear.

From the real space images we find that for early times following the almost instantaneous phase separation rapid coalescence of droplets takes place. This process gives rise to the formation of droplets with an area that is twice as large as that of the initial ones. This gives rise to a second length scale that exceeds the initial one by a factor of $\sqrt{2}$, consistent with the approximate ratio of the peak positions. For later times, the predominant wavenumber seems to decrease with the one-third power of time, indicating late-stage coarsening taking over. In conclusion, we put forward that initially rapid droplet coalescence takes place after which we enter the regime of Ostwald ripening.

How the various length scales develop with time and how they are affected by the rate of evaporation we discuss next. As we shall see, a unified picture emerges for all mixtures I–VI, at least for early times. For late times, we find that structure formation in asymmetric mixtures may differ from that in symmetric ones.

UNIVERSALITY AT THE EARLY STAGES OF DEMIXING

As we have seen in the previous section, evaporation-driven phase separation in solvent-borne polymer blends is characterized by two kinetic regimes. The transition between these two regimes coincides with the lag time, τ_L, to bifurcation, i.e., to rapid demixing. We find this for all mixtures I–VI (Table 1) and evaporation rates that we studied. For short times, $t < \tau_L$, we have spinodal decomposition, but not as we know it due to the ongoing evaporation. In this section we analyze spinodal decomposition under steady evaporation by applying a linearized theory. We calculate how the spinodal wavenumber increases with time and deduce from that a time scale that we can connect to the lag time τ_L. The theory allows us to approximately collapse the numerical results of all mixtures

DOI: 10.1021/acs.macromol.6b00537
Macromolecules 2016, 49, 6858–6870

onto a single master curve, showing near universality of both the symmetric and asymmetric mixtures.

The key assumptions of our approximate evaluation of our dynamic equation are (i) the variations in concentration and composition are small in the early stages and (ii) that solvent partitioning does not influence the early stage dynamics. The latter assumption implies that *cooperative diffusion*, i.e., the process associated with amplification of *concentration fluctuations* (for $t > 0$), is unimportant and that *interdiffusion*, i.e., the process associated with the amplification of *composition fluctuations*, prevails. Hence, in eq 11 we set the solvent current $\mathbf{j}_S$ to zero, implying that $\mathbf{j}_A = -\mathbf{j}_B$ and that the total concentration of solutes remains spatially uniform, but increases with time as $\phi(t) = \phi_0 + \alpha t$ with ϕ_0 the spinodal concentration that we cross at $t = 0$.

Under these assumptions, we can express the mass current as

$$\mathbf{j}_A = -\Lambda\nabla(\Delta\mu_A - \Delta\mu_B) \tag{20}$$

where $\Lambda = \Lambda_A\Lambda_B/(\Lambda_A + \Lambda_B)$ is the slow-mode mobility coefficient and $\kappa \equiv \kappa_{AA} + \kappa_{BB} - 2\kappa_{AB} > 0$ is an effective concentration-gradient stiffness. As discussed previously, we write the bare mobilities as $\Lambda_m = \phi_m N_m D_m$ with D_m the tracer diffusivity of polymer m that we take constant, so that at high dilution, $\phi_m \to 0$, we retain Fickian diffusion, $\mathbf{j}_m = -D_m\nabla\phi_m$ for m = A, B, and S that respectively holds for low concentrations of polymer A, polymer B, or solvent.

If we now introduce the transformation of variables $(\phi_A(\mathbf{r},t), \phi_B(\mathbf{r},t)) \to (\phi(t), \nu(\mathbf{r},t))$, with $\nu \equiv \phi_A/(\phi_A + \phi_B)$ the composition and $\phi \equiv \phi_A + \phi_B$ the concentration, we obtain

$$\mathbf{j}_A = -\Lambda\nabla\left(\frac{1}{\phi}\frac{\partial f_{loc}}{\partial\nu} - \kappa\phi\nabla^2\nu\right) \tag{21}$$

Here, we have made use of the exchange chemical potentials in eqs 6 and 7.

It is now expedient to express the local free energy density in eq 21 in terms of a free energy per solute segment, $\tilde{f}_{loc}$, as $f_{loc} \equiv \phi\tilde{f}_{loc}$. This quantity obeys

$$\tilde{f}_{loc} = \frac{1}{N_A}\nu\ln\nu + \frac{1}{N_B}(1-\nu)\ln(1-\nu) - \nu^2\phi\chi_{AB} + ... \tag{22}$$

where we have discarded all terms independent of ν as well as those linear in ν, as these do not contribute to the mass current. Note that eq 22 illustrates why our mixtures become unstable: the concentration and therefore the effective interaction parameter, $\phi\chi_{AB}$, increase due to steady evaporation.

To finally obtain the approximate generalized diffusion equation, we substitute the local free energy of eq 22 into eq 20 and subsequently insert this into the continuity equation $\partial_t\phi_A + \nabla\cdot\mathbf{j}_A = 0$, giving

$$\partial_t\phi = \nabla\cdot\Lambda\nabla(\partial_\nu\tilde{f}_{loc} - \kappa\phi\nabla^2\nu) \tag{23}$$

with the concentration $\phi = \phi_0 + \alpha t$ and with composition field $\nu = \nu(\mathbf{r},t)$. Note that $\Lambda = \Lambda(\nu(\mathbf{r},t), \phi(t))$ depends on the spatial coordinate and on time. We reiterative that $\nu(\mathbf{r},t) = \nu_0 + \delta\nu(\mathbf{r},t)$ with ν_0 the overall spinodal composition at $t = 0$ and $\delta\nu$ the time- and position-dependent spatial deviation from it.

For early times, after entering the spinodal region at $t = 0$, the composition fluctuations remain small, allowing us to linearize the diffusion equation and obtain

$$\partial_t\delta\nu(\mathbf{r},t) = M_0\nabla^2(\partial_\nu\tilde{f}_{loc}|_{\nu_0}(t) - \kappa\phi(t)\nabla^2)\delta\nu(\mathbf{r},t) \tag{24}$$

with $M_0 \equiv \Lambda/\phi_0$ a renormalized mobility coefficient at the spinodal concentration, given by

$$M_0 = \nu_0 N_A D_A(1-\nu_0)N_B D_B/(\nu_0 N_A D_A + (1-\nu_0)N_B D_B) \tag{25}$$

which is independent of the overall solute concentration.

The spatial Fourier transformation of the linearized equation reads

$$\partial_t\delta\hat{\nu}(q,t) = -q^2 M_0(\partial_\nu\tilde{f}_{loc}|_{\nu_0}(t) + \kappa\phi(t)q^2)\delta\hat{\nu}(q,t) \tag{26}$$

with $q = |\mathbf{q}|$ the magnitude of the momentum transfer and $\delta\hat{\nu}$ the Fourier transform of $\delta\nu$. From eq 22 we find given that at the spinodal $\partial_{\nu\nu} + \tilde{f}_{loc}|_{\nu_0}(0) = 0$ holds, that $\partial_{\nu\nu} + \tilde{f}_{loc}|_{\nu_0}(t) = -2\chi_{AB}\alpha t$, with α the constant evaporation rate.

Integration of eq 26 over time yields

$$\ln\frac{\delta\hat{\nu}(q,t)}{\delta\hat{\nu}(q,0)} = -R(q,t)t \tag{27}$$

with relaxation rate

$$R(q,t) = q^2 M_0\left(-\chi_{AB}\alpha t + \kappa\left(\phi_0 + \frac{1}{2}\alpha t\right)q^2\right) \tag{28}$$

and ϕ_0 (again) the spinodal concentration at time $t = 0$.

Inspection of eq 28 shows that immediately after crossing the spinodal the relaxation rate is positive for short-wavelength fluctuations. This implies that they relax. The opposite is true for long-wavelength fluctuations, for which the relaxation rate is negative and hence spontaneous fluctuations grow in amplitude. The amplification is slow because mass transport has to take place over large distances, and the composition variations remain small, $|\delta\nu| \ll \nu_0$. As time progresses, the relaxation rate also becomes negative for smaller wavelengths. Hence, the system becomes further destabilized, and the critical length scale for fluctuation amplification decreases with time. This confirms what we found numerically in Figure 4.

We obtain the corresponding time-dependent spinodal length by maximizing eq 28, giving

$$q_*(t) = \sqrt{\frac{\chi_{AB}\alpha t}{\kappa(2\phi_0 + \alpha t)}} \tag{29}$$

In Figure 4 we compare this expression (solid line) with our numerically obtained results (filled triangles) for $t < \tau_L$. We indeed obtain excellent agreement between the numerically generated data and the prediction from linearized theory.

For short times, $t \ll 2\phi_0/\alpha$, we find that the wavenumber grows with the square root of time, $q_*(t) \approx \sqrt{\chi_{AB}\alpha t/2\phi_0\kappa}$. For long times, $t \gg 2\phi_0/\alpha$, the wavenumber becomes time independent, $q_* \propto \sqrt{\chi_{AB}/\kappa}$, and asymptotes to the value obtained for a classical temperature quench of a binary polymer mixture without a solvent.

Now that we understand how the evaporation rate affects the spinodal length scale, it makes sense to investigate evaporation affects the growth rates of the most unstable mode. For this purpose we evaluate eq 27 at the spinodal wavenumber given by eq 29. First, we insert eq 29 for $q_*(t)$ in the expression for the amplification rate, R, in eq 28, giving

DOI: 10.1021/acs.macromol.6b00537
Macromolecules 2016, 49, 6858−6870

$$R(q_*(t), t) = -\kappa(\phi_0 + (1/2)\alpha t)M_0 q_*^4(t) \tag{30}$$

which is zero at $t = 0$ but becomes negative with time. The maximum growth rate of fluctuations apparently grow with the square of the evaporation rate and time for times $t < 2\phi_0/\alpha$ but slows down to a linear dependence on evaporation rate and time for times $t > 2\phi_0/\alpha$.

Our predictions for the spinodal length scale equation in eq 29 and the maximum amplification rate in eq 30 break down at the point where $|\delta\nu| \approx \nu_0$. This allows us to estimate at what point nonlinear effects become important, nonlinear effects that lead to the rapid separation of phases after the lag time τ_L. This means we can use eqs 29 and 30 to estimate that lag time.

Inserting eqs 29 and 30 into eq 27 and inserting τ_L for the time t gives

$$\ln r_L = \kappa\left(\phi_0 + \frac{1}{2}\alpha\tau_L\right)M_0\left(\frac{\chi_{AB}\alpha\tau_L}{\kappa(2\phi_0 + \alpha\tau_L)}\right)^2\tau_L \tag{31}$$

Here, $r_L = \delta\hat{\nu}(q_*(\tau_L), \tau_L)/\delta\hat{\nu}(q_*(\tau_L), 0)$ is a measure for the maximum amplification of composition fluctuations at what we identify as the crossover to the coarsening regime. Because of the logarithmic dependence, this lag time is only weakly affected by the value of r_L. Plausibly the amplification factor in Fourier space is the same as that in real space, and because of the logarithmic dependence we need not to compare the magnitude of the fluctuation to the composition at the spinodal.

For all intents and purposes the left-hand side of eq 31 is a constant of τ_L. This means that the right-hand side depends on the evaporation rate and the various other parameters. For this reason, we treat r_L as a fitting parameter and use eq 31 to establish how our numerically obtained values for τ_L depend on the evaporation rate α and all the other parameters for all mixtures studied.

Comparison with our numerical data shows that the lag time τ_L and associated wavenumber $q_*(\tau_L)$ that we calculate from our linearized theory do indeed correlate with those of the emerging structure at the moment of composition bifurcation. For sufficiently slow solvent evaporation, $\alpha\tau_L \ll 2\phi_0$, the lag time obeys

$$\tau_L^3 \sim (\kappa\phi_0/M_0)(1/\chi_{AB}\alpha)^2 \tag{32}$$

which confirms the weak dependence of the lag time on r_L: $\tau_L \propto \sqrt[3]{\ln r_L}$.

Equation 32 points at the existence of two natural time scales. The first, $\tau_d \equiv \kappa\phi_0/\Lambda$, is associated with phase separation by interdiffusion over a characteristic distance $\sqrt{\kappa\phi_0}$. The second time scale, $\tau_e \equiv 1/\chi_{AB}\alpha = 2/|\partial_t \partial_{\nu\nu} + \tilde{f}_{loc}|_{\nu_0}|$, is associated with the rate at which the mixture is destabilized by evaporation. Hence, faster diffusion and faster evaporation give rise to a decrease of the lag time. In fact, from eq 32 we find that the lag time can be written as

$$\tau_L \propto \tau_d^{1/3}\tau_e^{2/3} \tag{33}$$

and the emerging structural wavenumber at the lag time as

$$q_*(\tau_L) \propto \frac{1}{\sqrt{\kappa\phi_0}}\left(\frac{\tau_d}{\tau_e}\right)^{1/6} \equiv \frac{1}{\sqrt{\kappa\phi_0}}\tilde{\alpha}^{1/6} \tag{34}$$

with $\tilde{\alpha} \equiv \tau_d/\tau_e$ the dimensionless evaporation rate.

Equations 32−34 hold for sufficiently slow evaporation. This is true if $\alpha\tau_L \ll 2\phi_0$, or, in dimensionless units, if $\tilde{\alpha} \ll 8\phi_0^3\chi_{AB}^3$ holds. Under this condition the wavenumber and lag time respectively scale with the 1/6 and the −2/3 power of the evaporation rate. For fast evaporation, i.e., $\tilde{\alpha} \gg 8\phi_0^3\chi_{AB}^3$, the wavenumber and lag time respectively scale with the zeroth and the −1/2 power.

We have verified these findings by numerically solving the generalized diffusion equations in eqs 17 and 18 for the host of parameter values given in Table 1. Figure 5 indeed shows that

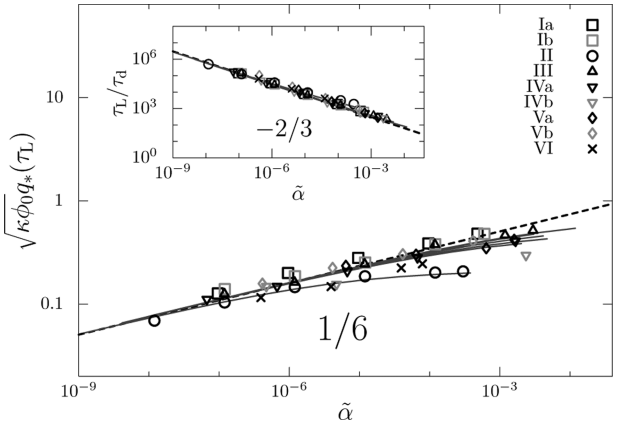

Figure 5. Emerging structural wavenumber $q_*(\tau_L)$ (main figure) at the crossover from the early to the late stages of demixing and the lag time τ_L (inset) at which this crossover appears as a function of dimensionless evaporation rate $\tilde{\alpha}$. We have rendered the units dimensionless using the length $\sqrt{\phi_0\kappa}$ and the time scale τ_d of interdiffusion. The numerical results (symbols) are curve fitted with a single parameter from the linearized theory in eq 31 (solid lines) and approach limiting power laws (dashed lines) for slow evaporation, $\tilde{\alpha} \ll 8\phi_0^3\chi_{AB}^3$. In this limit, the wavenumber and lag time respectively scale with the 1/6 and the −2/3 power of evaporation rate. For fast evaporation, $\tilde{\alpha} \gg 8\phi_0^3\chi_{AB}^3$, the wavenumber and lag time respectively scale with the zeroth and the −1/2 power. The various system parameters are given in Table 1.

the numerically found (symbols) typical wavenumber of the emerging structure at the lag time as well as the lag time itself correspond to this linearized theory (solid lines). This confirms our assumptions that (i) prior to the lag time the composition fluctuations remain relatively small and (ii) the influence of concentration fluctuations is negligible in that regime. These findings show that we have a good understanding of early stage spinodal demixing of ternary mixtures under the action of evaporation and are able to predict the lag time and the corresponding predominant wavenumber. In the next section we discuss how evaporation influences the coarsening dynamics during the late stages of demixing.

EFFECT OF EVAPORATION ON LATE-STAGE COARSENING

To what extent the final dry-layer morphology resembles the emerging structure depends on its evolution during the late stages of phase separation, as already discussed. This influence is largely determined by the time available to structure development, which is set by the evaporation rate. Evaporation not only determines the time period of coarsening but may also affect the coarsening mechanism itself. That this must be so is evident from Figures 2 and 3 which show that morphological

DOI: 10.1021/acs.macromol.6b00537
Macromolecules 2016, 49, 6858−6870

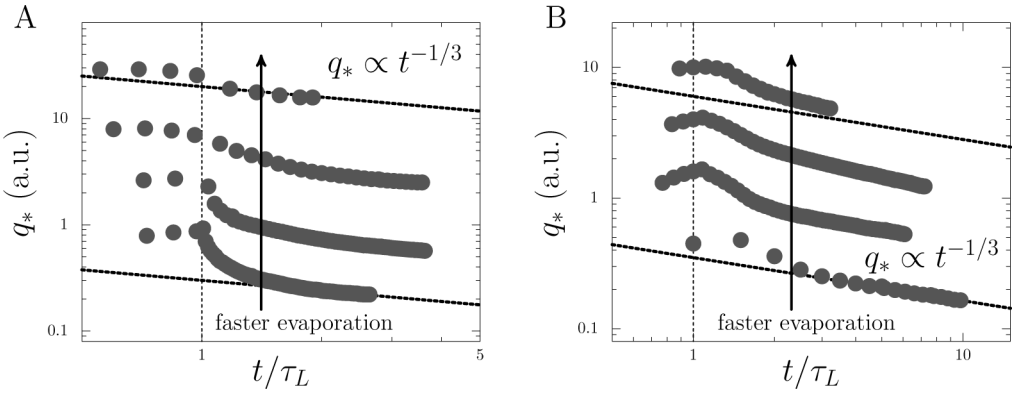

Figure 6. Time evolution of the predominant structural wavenumber, q_*, that characterizes a symmetric (A) and an asymmetric (B) mixture. The parameters of mixtures respectively II and IV(b) are as given in Table 1 for rates of solvent evaporation $\tilde{\alpha} = 1.2 \times 10^{-7}$–$1.2 \times 10^{-3}$ and 4.7×10^{-7}–4.7×10^{-3}, respectively. For clarity the curves for different evaporation rates have been shifted parallel to the vertical axis.

transients, i.e., structural changes during the late stages, can indeed be observed. This is especially true if the volume ratio of the coexisting phases is strongly time dependent. As shown, the volume ratio becomes time dependent for sufficiently fast evaporation in combination with an appropriate blend composition and pronounced asymmetry of the phase diagram.

In this section, we quantify how the morphological transients, as observed for mixture IV(b), affect the time evolution of the associated structural length scales. We achieve this by comparing the coarsening dynamics of mixture IV(b) with that of mixture II, for which we do not expect such transients because of its highly symmetric phase diagram (see Figure 1). The coarsening dynamics for mixture II is hence not expected to be influenced by evaporation, but rather to obey classical behavior. Its phase-separated morphology is dispersed due to the off-critical 1:2 solute ratio, and should therefore coarsen via Ostwald ripening, i.e., growth of large droplets at the expense of small ones to reduce interfacial free energy. For this mode of coarsening Lifshitz–Slyozov–Wagner (LSW) theory predicts the average domain size to increase with the one-third power of time, both in two and three spatial dimensions (except for a logarithmic correction in 2D).[55,56] Notably, as the classical time evolution of the structural wavenumber characterizing the phase-separated morphology must rely on a fixed volume ratio of the coexisting phases, deviation from it is likely to occur once morphological transients are present.

We obtain the time dependence of the structural wavenumbers for mixtures II and IV(b) by solving the generalized diffusion equations for various evaporation rates. In Figure 6 we present the calculated predominant wavenumber (symbols) as a function of time for the symmetric (A) and asymmetric (B) cases. The dotted lines indicate the classical one-third time exponent. We indeed find that at long times for slow evaporation the coarsening kinetics of both mixtures are consistent with the LSW theory. In contrast, as expected from the morphological transients expressed by Figure 3, consistency with LSW theory is not achieved for fast evaporation of solvent from mixture IV(b) (Figure 6B). We note that the numerical calculation corresponding to the highest evaporation rate was performed until dryness was reached.

In conclusion, late-stage coarsening in highly asymmetric phase-separated mixtures loses universality in the limit of fast evaporation. We attribute this to incomplete structural relaxation within the time period available to coarsening.

DISCUSSION AND CONCLUSION

Thin solvent-cast polymer-composite films find application in organic photovoltaics.[17,27] We have applied a quasi-two-dimensional generalized diffusion model to describe how evaporation drives the lateral phase separation of the two solute components, which act as an electron donor and acceptor in such films. Our model applies to those casting conditions where no vertical, substrate- or evaporation-driven, stratification takes place. We have considered various practical mixtures where the two components have a different solubility in the solvent but also various idealized symmetric mixtures where the two solutes do have the same solubility. We find that whether or not the mixture is symmetric has no impact on the early stage kinetics of phase separation. In the early stages of phase separation, evaporation leads to a spinodal length that decreases with time. This contrasts with the classical case of an instantaneous quench, where the spinodal length is independent of time.

At the end of the spinodal-like early stages a sharp crossover takes place, where the compositions of the coexisting phases rapidly approach their binodal values. At the crossover a structure emerges of which the characteristic length scale decreases with the one-sixth power of the evaporation rate, for both symmetric and asymmetric mixtures. The emerging structure can either be dispersed or bicontinuous. For symmetric mixtures this type of morphology is solely determined by the blend ratio of the solutes. In contrast, for asymmetric mixtures the emerging morphology strongly depends on the concentration at which the crossover takes place. This concentration is determined by the rate of evaporation.

To what extent the dry-layer morphology resembles this emerging structure depends on the structure development during the late stages of phase separation. For increasingly slow evaporation, an increasing extent of structure development is possible because more time for coarsening is available. Under the condition of slow evaporation, the predominant structural length seems to increase with the classical one-third power of time. For fast evaporation, deviations from universal behavior may present themselves, especially if the solubility of the solute components differs. We conclude that the rate of evaporation controls both the type of morphology and its characteristic length scale.

We find qualitative agreement between the structure of our laterally phase-separated solutions with the ones obtained

DOI: 10.1021/acs.macromol.6b00537
Macromolecules 2016, 49, 6858–6870

experimentally for mixtures IV and V discussed in the main text, at least if we presume low evaporation rates.[17,27] In that case we find droplets consisting mainly of the fullerene-based material in a continuum of the electron-donating polymer. In this limit, we find from our model calculations that rapid phase separation occurs near the spinodal concentration. This agrees with the experiments, where *in situ* light scattering reveals a significant increase of the intensity near a concentration that is consistent with our predictions for the mixture in hand. In addition, the observed structural length scale of the dry-layer film increases with the one-third power of the evaporation rate. This is consistent with the coarsening-dynamics dictated length scale that dominates the late stages under slow evaporation.

Our model calculations do not seem to agree with the experimental findings for mixture VI.[27] Nilsson et al. find for that mixture a layered structure perpendicular to the substrate. This already indicates that stratification has taken place and hence that the conditions of the experiments are outside the validity of our theory. Indeed, our model is valid only in the limit of small Biot numbers, i.e., under conditions where the diffusive mass transport in the film counteracts concentration accumulation near the top surface of the evaporating film. In the experiments of Nilsson et al. for mixture VI, phase separation does not take place at low concentrations, as is the case for the experiments on mixtures IV and V. At high concentrations, the tracer diffusivities of the various solutes are substantially lower due to caging, suggesting that diffusion cannot keep up with the advancing interface. So, we surmise that in experiments on mixture VI the Biot number is large not small, and hence our theory does not apply.

Our findings strongly suggest that experimental control is possible over the final morphology of the film by controlling the evaporation rate and blend composition. Indeed, transitions between thermodynamics-dictated dispersed morphologies and kinetics-dictated inverse or bicontinuous morphologies can be achieved. Maximum control over the morphology is possible if the polymer−polymer blend ratio is chosen to be close to the critical ratio and if the solvent is chosen such that the solubility of the two solutes in it is sufficiently different. Given the importance of morphologies to e.g. solar cell and membrane technology, our hope is that our work will inspire experimental follow up to explore this further.

APPENDIX. NUMERICAL IMPLEMENTATION

In order to numerically solve the stochastic generalized diffusion equation of eqs 17 and 18, we discretize the fluctuation−dissipation theorem in eq 19

$$\langle \zeta_m(\mathbf{r}, t)\rangle = 0,$$
$$\langle \zeta_m(\mathbf{r}, t)\zeta_n(\mathbf{r}', t')\rangle = -2\nabla\Lambda_{mn}\nabla\delta(\mathbf{r}-\mathbf{r}')\delta(t-t') \quad (35)$$

where the index m, n = A, B is the label of a component in the mixture, t time, Λ_{mn} the mobility coefficient of components m, n = A and B, δ the Dirac-delta distribution, and $\mathbf{r}$ the position in 2D space that on a square two-dimensional grid we discretize as $\mathbf{r}_{ij} = [x_i + y_j]^T$ for $i, j = 1, 2, ..., N_{grid}$ with N_{grid} the grid size. On a square lattice the positional coordinate is $[x_i + y_j]^T = [i - 1\ j - 1]^T\Delta x$ with Δx the lattice spacing. Here, we obtain the thermal fluctuations by adopting a method by Petschek and Metiu that they used for binary mixtures with constant mobility and generalize this for ternary mixtures with concentration-dependent mobility.[57] In this method, spatially correlated noise fields are generated from common uncorrelated random numbers.

First, we factorize the Dirac delta distribution as $\delta(\mathbf{r}-\mathbf{r}') = \delta(x-x')\delta(y-y')$ and discretize the coordinates $(x, y) \to (x_i, y_j)$, $(x', y') \to (x_k, y_l)$ to obtain $\delta(\mathbf{r}-\mathbf{r}') = \delta(x_i - x_k)\delta(y_j - y_l)$. We use central difference to approximate the gradient by $\mathrm{d}\delta(x_i - x_k)/\mathrm{d}x \approx (\delta(x_i + \Delta x/2 - x_k) - \delta(x_i - \Delta x/2 - x_k))/\Delta x = (\delta(x_{i+1/2} - x_k) - \delta(x_{i-1/2} - x_k))/\Delta x$ and subsequently introduce the Kronecker delta function $\delta_{ik} \equiv \delta(x_i - x_k)/\Delta x$ to obtain $\mathrm{d}\delta(x_i - x_k)/\mathrm{d}x \approx (\delta_{(i+1/2)k} - \delta_{(i-1/2)k})/(\Delta x)^2$. In order to obtain the gradient of $\delta(\mathbf{r}-\mathbf{r}')$, we do the same for the y coordinate, giving

$$\mathbf{g}_{ij} \equiv (\Lambda_{mn}\nabla\delta(\mathbf{r}-\mathbf{r}'))_{ij} \approx \frac{\Lambda^{ij}_{mn}}{\Delta x^3}\begin{pmatrix}[\delta_{(i+\frac{1}{2})k} - \delta_{(i-\frac{1}{2})k}]\delta_{jl}\\ [\delta_{(j+\frac{1}{2})l} - \delta_{(j-\frac{1}{2})l}]\delta_{ik}\end{pmatrix} \equiv [g^x_{ij} g^y_{ij}]^T \quad (36)$$

where (i, j) and (k, l) are positions on the lattice.

Now, to obtain the discretized divergence, $\nabla\cdot\Lambda_{mn}\nabla\delta(\mathbf{r}-\mathbf{r}')\delta(t-t')$, we apply central difference of the form $\nabla\cdot\mathbf{g}_{ij} \approx (g^x_{(i+1/2)j} - g^x_{(i-1/2)j})/\Delta x + (g^y_{(i+1/2)j} - g^y_{(i-1/2)j})/\Delta x$. This gives the discretized version of the fluctuation−dissipation theorem as

$$\langle \zeta^m_{ij}\zeta^n_{kl}\rangle = -2\sigma^2\{[\Lambda^{(i+1/2)j}_{mn}(\delta_{(i+1)k} - \delta_{ik}) - \Lambda^{(i-1/2)j}_{mn} \times (\delta_{ik} - \delta_{(i-1)k})]\delta_{jl} + [\Lambda^{i(j+1/2)}_{mn}(\delta_{(j+1)l} - \delta_{jl}) - \Lambda^{i(j-1/2)}_{mn}(\delta_{jl} - \delta_{(j-1)l})]\delta_{ik}\} \quad (37)$$

with $\sigma^2 \equiv (1/\Delta x)^2(\Delta t/\Delta x^2)$. Note that $(\Delta x)^2$ is the number of segments per coarse-grained cell, so that a smaller Δx implies larger fluctuations. Finally, we cast the discretized fluctuation−dissipation theorem in the form

$$\langle \zeta^m_{ij}\zeta^n_{kl}\rangle = 2\sigma^2\{[\Lambda^{(i+1/2)j}_{mn} + \Lambda^{(i-1/2)j}_{mn} + \Lambda^{i(j+1/2)}_{mn} + \Lambda^{i(j-1/2)}_{mn}]\delta_{ik}\delta_{jl} - \Lambda^{(i+1/2)j}_{mn}\delta_{(i+1)k}\delta_{jl} - \Lambda^{(i-1/2)j}_{mn}\delta_{(i-1)k}\delta_{jl} - \Lambda^{i(j+1/2)}_{mn}\delta_{ik}\delta_{(j+1)l} - \Lambda^{i(j-1/2)}_{mn}\delta_{ik}\delta_{(j-1)l}\} \quad (38)$$

where we have approximated the mobility coefficients by

$$\Lambda^{(i\pm1/2)j}_{mn} = \frac{1}{2}(\Lambda^{ij}_{mn} + \Lambda^{(i\pm1)j}_{mn}),$$
$$\Lambda^{i(j\pm1/2)}_{mn} = \frac{1}{2}(\Lambda^{ij}_{mn} + \Lambda^{i(j\pm1)}_{mn}) \quad (39)$$

We generate these correlated noise fields with a method similar to that of Petschek et al.[57] In both our and in their work uncorrelated fields are defined, which are spatially correlated by introducing displacements in x and y directions. In eqs 13a and 13b of their work, they have introduced uncorrelated fields that have zero mean and a variance that is determined by the mobility M (which roughly corresponds to Λ in our work). We find that this does not lead to the correct correlated fluctuations in case the mobility depends on concentration. Here, we let the variance of the uncorrelated fields, $\xi \in \{\nu^A, \nu^B, \mu^A, \mu^B, \gamma, \eta\}$, be determined by the variance σ^2 (which roughly corresponds to h^2 in their work) via

$$\langle \xi_{ij}\xi_{kl}\rangle = 2\sigma^2\delta_{ik}\delta_{jl} \quad (40)$$

DOI: 10.1021/acs.macromol.6b00537
Macromolecules 2016, 49, 6858−6870

and introduce the mobility at the point that the fields are being correlated.

We correlate these fields in correspondence with eq 12 of the work of Petschek et al., which is now more involved due to the concentration-dependent mobility. Unfortunately, starting from the desired result in eq 38, we can not derive an expression for the spatially correlated fields ζ in terms of the uncorrelated fields ξ. By trial we have found the desired results in the form of the expressions

$$\begin{aligned}\zeta_{ij}^{\mathrm{A}} = {} & \sqrt{\Lambda_{\mathrm{AA}}^{(i+1/2)j} - |\Lambda_{\mathrm{AB}}^{(i+1/2)j}|}\,\nu_{(i+1)j}^{\mathrm{A}} + \sqrt{|\Lambda_{\mathrm{AB}}^{(i+1/2)j}|}\,\gamma_{(i+1)j} \\ & - \sqrt{\Lambda_{\mathrm{AA}}^{(i-1/2)j} - |\Lambda_{\mathrm{AB}}^{(i-1/2)j}|}\,\nu_{ij}^{\mathrm{A}} - \sqrt{|\Lambda_{\mathrm{AB}}^{(i-1/2)j}|}\,\gamma_{ij} \\ & + \sqrt{\Lambda_{\mathrm{AA}}^{i(j+1/2)} - |\Lambda_{\mathrm{AB}}^{i(j+1/2)}|}\,\mu_{i(j+1)}^{\mathrm{A}} + \sqrt{|\Lambda_{\mathrm{AB}}^{i(j+1/2)}|}\,\eta_{i(j+1)} \\ & - \sqrt{\Lambda_{\mathrm{AA}}^{i(j-1/2)} - |\Lambda_{\mathrm{AB}}^{i(j-1/2)}|}\,\mu_{ij}^{\mathrm{A}} - \sqrt{|\Lambda_{\mathrm{AB}}^{i(j-1/2)}|}\,\eta_{ij} \end{aligned} \tag{41}$$

and

$$\begin{aligned}\zeta_{ij}^{\mathrm{B}} = {} & \sqrt{\Lambda_{\mathrm{BB}}^{(i+1/2)j} - |\Lambda_{\mathrm{AB}}^{(i+1/2)j}|}\,\nu_{(i+1)j}^{\mathrm{B}} + \mathrm{sgn}(\Lambda_{\mathrm{AB}}^{(i+1/2)j})\sqrt{|\Lambda_{\mathrm{AB}}^{(i+1/2)j}|}\,\gamma_{(i+1)j} \\ & - \sqrt{\Lambda_{\mathrm{BB}}^{(i-1/2)j} - |\Lambda_{\mathrm{AB}}^{(i-1/2)j}|}\,\nu_{ij}^{\mathrm{B}} - \mathrm{sgn}(\Lambda_{\mathrm{AB}}^{(i-1/2)j})\sqrt{|\Lambda_{\mathrm{AB}}^{(i-1/2)j}|}\,\gamma_{ij} \\ & + \sqrt{\Lambda_{\mathrm{BB}}^{i(j+1/2)} - |\Lambda_{\mathrm{AB}}^{i(j+1/2)}|}\,\mu_{i(j+1)}^{\mathrm{B}} + \mathrm{sgn}(\Lambda_{\mathrm{AB}}^{i(j+1/2)})\sqrt{|\Lambda_{\mathrm{AB}}^{i(j+1/2)}|}\,\eta_{i(j+1)} \\ & - \sqrt{\Lambda_{\mathrm{BB}}^{i(j-1/2)} - |\Lambda_{\mathrm{AB}}^{i(j-1/2)}|}\,\mu_{ij}^{\mathrm{B}} - \mathrm{sgn}(\Lambda_{\mathrm{AB}}^{i(j-1/2)})\sqrt{|\Lambda_{\mathrm{AB}}^{i(j-1/2)}|}\,\eta_{ij} \end{aligned} \tag{42}$$

where the ν and γ fields generate correlations in the i (x) direction and the μ and η fields generate correlations in the j (y) direction. The γ and η fields correlate the noise fields of the two different components. In this equation sgn is the sign function, which is 1 for positive cross-mobility Λ_{AB}, −1 for negative cross-mobility, and 0 otherwise. By taking the product $\langle \zeta_{ij}^{m} \zeta_{kl}^{n} \rangle$, we find after some algebra that this indeed results in eq 38. If one discards the cross mobilities $\Lambda_{\mathrm{AB}} = 0$ and assumes that the other mobilities are position independent, this expression reduces to the one given by Petschek and Metiu.[57] Generalization of this result to systems with more than three components and to systems with a higher or dimensionality is straightforward.

AUTHOR INFORMATION

Corresponding Author

*E-mail: c.schaefer@tue.nl (C.S.).

Notes

The authors declare no competing financial interest.

ACKNOWLEDGMENTS

This research forms part of the research program of the Dutch Polymer Institute (DPI), project #734. The authors thank M. A. J. Michels and J. J. van Franeker for useful discussions.

ADDITIONAL NOTES

[a]We note that the Biot number is a dimensionless quantity that compares the rate of external mass transport by evaporation to that of internal mass transport by diffusion. Because our solutes need not have equal diffusivities, we have one Biot number for every solute.

[b]Strictly speaking, even if we ignore local variations and the solvent evaporation rate is proportional to the overall concentration of solvent, $\alpha \propto \phi^2(1-\phi)$.[43] For short times after entering the spinodal this can be considered constant.

[c]The binodal and tie-lines lines have been obtained using the common tangent construction,[54] which involves equating the local exchange chemical potentials of coexisting phases I and II and the osmotic pressures according to $\mu_{\mathrm{loc,m}}^{0} \equiv \mu_{\mathrm{loc,m}}^{\mathrm{I}} = \mu_{\mathrm{loc,m}}^{\mathrm{II}}$ for m = A, B and $f_{\mathrm{loc}}^{\mathrm{II}} = f_{\mathrm{loc}}^{\mathrm{I}} + \mu_{\mathrm{loc,A}}^{0}(\phi_{\mathrm{A}}^{\mathrm{II}} - \phi_{\mathrm{A}}^{\mathrm{I}}) + \mu_{\mathrm{loc,B}}^{0}(\phi_{\mathrm{B}}^{\mathrm{II}} - \phi_{\mathrm{B}}^{\mathrm{I}})$. The spinodal lines, which separate the metastable and unstable regions, have been obtained by solving $(\partial_{\phi_{\mathrm{A}}\phi_{\mathrm{A}}} f_{\mathrm{loc}})(\partial_{\phi_{\mathrm{B}}\phi_{\mathrm{B}}} f_{\mathrm{loc}}) - (\partial_{\phi_{\mathrm{A}}\phi_{\mathrm{B}}} f_{\mathrm{loc}})^2 = 0$.

[d]Here, the term lag time, τ_{L}, is not to be confused with the lag time from classical nucleation theory.[26]

REFERENCES

(1) Deibel, C.; Dyakonov, V. Polymer-fullerene bulk heterojunction solar cells. *Rep. Prog. Phys.* **2010**, *73*, 096401.

(2) Brabec, C. J.; Gowrisanker, S.; Halls, J. J. M.; Laird, D.; Jia, J.; Williams, S. P. Spin coating of a PMMA/chlorobenzene solution. *Adv. Mater.* **2010**, *22*, 3839−3856.

(3) Nelson, J. Polymer:fullerene bulk heterojunction solar cells. *Mater. Today* **2011**, *14*, 462−470.

(4) Greenham, N. C. Polymer solar cells. *Philos. Trans. R. Soc. A* **2013**, *13*, 371−381.

(5) Asadi, K.; de Leeuw, D. M.; de Boer, B.; Blom, P. W. M. Organic non-volatile memories from ferroelectric phase-separated blends. *Nat. Mater.* **2008**, *7*, 547−550.

(6) Asadi, K.; Wondergem, H. J.; Moghaddam, R. S.; McNeill, C. R.; Wondergem, H. J.; Stingelin, N.; Noheda, B.; Blom, P. W. M.; de Leeuw, D. M. Spinodal decomposition of blends of semiconducting and ferroelectric polymers. *Adv. Funct. Mater.* **2011**, *21*, 1887−1894.

(7) Li, M.; Stingelin, N.; Michels, J. J.; Spijkman, M. J.; Asadi, K.; Beerends, R.; Biscarini, F.; Blom, P. W. M.; de Leeuw, D. M. Processing and low voltage switching of organic ferroelectric phase-separated bistable diodes. *Adv. Funct. Mater.* **2012**, *22*, 2750−2757.

(8) Khikhlovskyi, V.; Wang, R.; van Breemen, A. J. J. M.; Gelinck, G. H.; Janssen, R. A. J.; Kemerink, M. Nanoscale organic ferroelectric resistive switches. *J. Phys. Chem. C* **2014**, *118*, 3305−3312.

(9) Hwang, D. K.; Fuentes-Hernandez, J. D.; Fang, Y.; Kim, J.; Potscavage, W. J.; Cheun, H.; Sandhage, K. H.; Kippelen, B. Solvent and polymer matrix effects on TIPS-pentacene/polymer blend organic field-effect transistors. *J. Mater. Chem.* **2012**, *22*, 5531−5537.

(10) Niazi, M. R.; Li, R.; Li, E. Q.; Kirmani, A. R.; Abdelsamie, M.; Wang, Q.; Pan, W.; Payne, M. M.; Anthony, J. E.; Smilgies, D.-M.; Thoroddsen, S. T.; Giannelis, E. P.; Amassian, A. Solution-printed organic semiconductor blends exhibiting transport properties on par with single crystals. *Nat. Commun.* **2015**, *6*, 8598.

(11) van de Witte, P.; Dijkstra, P. J.; van den Berg, J. W. A.; Feijen, J. Phase separation processes in polymer solutions in relation to membrane formation. *J. Membr. Sci.* **1996**, *117*, 1−31.

(12) Ulbricht, M. Advanced functional polymer membranes. *Polymer* **2006**, *47*, 2217−2262.

(13) Liu, F.; Hashim, N. A.; Liu, Y.; Abed, M. R. M.; Li, K. Progress in the production and modification of PVDF membranes. *J. Membr. Sci.* **2011**, *375*, 1−27.

(14) Karagkiozaki, V.; Vavoulidis, E.; Karagiannidis, P. G.; Gioti, M.; Fatouros, D. G.; Vizirianakis, I. S.; Logothetidis, S. Development of a nanoporous and multilayer drug-delivery platform for medical implants. *Int. J. Nanomed.* **2012**, *7*, 5327−5338.

(15) Armentano, I.; Dottori, M.; Fortunati, E.; Mattioli, S.; Kenny, J. M. Biodegradable polymer matrix nanocomposites for tissue engineering: A review. *Polym. Degrad. Stab.* **2010**, *95*, 2126−2146.

(16) Kouijzer, S.; Michels, J.; van den Berg, M.; Gevaerts, V. S.; Turbiez, M.; Wienk, M. M.; Janssen, R. A. J. Predicting morphologies of solution processed polymer:fullerene blends. *J. Am. Chem. Soc.* **2013**, *135*, 12057−12067.

(17) van Franeker, J. J.; Westhoff, D.; Turbiez, M.; Wienk, M. M.; Schmidt, V.; Janssen, R. A. J. Controlling the dominant length scale of liquid-liquid phase separation in spin-coated organic semiconductor films. *Adv. Funct. Mater.* **2015**, *25*, 855−863.

DOI: 10.1021/acs.macromol.6b00537
Macromolecules 2016, 49, 6858−6870

(18) Walheim, S.; Böltau, M.; Mlynek, J.; Krausch, G.; Steiner, U. Structure formation via polymer demixing in spin-cast films. *Macromolecules* **1997**, *30*, 4995−5003.
(19) Dalnoki-Veress, K.; Forrest, J. A.; Stevens, J. R.; Dutcher, J. R. Phase separation morphology of spin-coated polymer blend thin films. *Phys. A* **1997**, *239*, 87−94.
(20) Zhang, H.; Takeoka, S. Morphological evolution within spin-cast ultrathin polymer blend films clarified by a freestanding method. *Macromolecules* **2012**, *45*, 4315−4321.
(21) Toolan, D. T. W.; Howse, J. R. Development of in situ studies of spin coated polymer films. *J. Mater. Chem. C* **2013**, *1*, 603−616.
(22) Glotzer, S. C.; Di Marzio, E. A.; Muthukumar, M. Reaction-controlled morphology of phase-separating mixtures. *Phys. Rev. Lett.* **1995**, *74*, 2034−2037.
(23) Christensen, J. J.; Elder, K.; Fogedby, H. C. Phase segregation dynamics of a chemically reactive binary mixture. *Phys. Rev. E: Stat. Phys., Plasmas, Fluids, Relat. Interdiscip. Top.* **1996**, *54*, R2212−R2215.
(24) Benmouna, F.; Bouabdellah-Dembahri, Z.; Benmouna, M. Polymerization-induced phase separation: Phase behavior developments and hydrodynamic interaction. *J. Macromol. Sci., Part B: Phys.* **2013**, *52*, 998−1008.
(25) Schaefer, C.; van der Schoot, P.; Michels, J. J. Structuring of polymer solutions upon solvent evaporation. *Phys. Rev. E* **2015**, *91*, 022602.
(26) Kashchiev, D. *Nucleation: Basic Theory with Applications*; Butterworth-Heinemann: Oxford, 2000.
(27) Nilsson, S.; Bernasik, A.; Budkowski, A.; Moons, E. Morphology and phase segregation of spin-casted films of polyfluorene/PCBM blends. *Macromolecules* **2007**, *40*, 8291−8301.
(28) Wodo, O.; Ganapathysubramanian, B. Modeling morphology evolution during solvent-based fabrication of organic solar cells. *Comput. Mater. Sci.* **2012**, *55*, 113−126.
(29) Wodo, O.; Ganapathysubramanian, B. How do evaporating thin films evolve? Unravelling phase-separation mechanisms during solvent-based fabrication of polymer blends. *Appl. Phys. Lett.* **2014**, *105*, 153104.
(30) de Groot, S. R.; Mazur, P. *Non-equilibrium Thermodynamics*; Dover Publications, Inc.: New York, 1984.
(31) de Gennes, P. G. Dynamics of fluctuations and spinodal decomposition in polymer blends. *J. Chem. Phys.* **1980**, *72*, 4756.
(32) Kramer, E. J.; Green, P.; Palmstrøm, C. J. Interdiffusion and marker movements in concentrated polymer-polymer diffusion couples. *Polymer* **1984**, *25*, 473−480.
(33) Flory, P. J. Thermodynamics of high polymer solutions. *J. Chem. Phys.* **1942**, *10*, 51−61.
(34) Flory, P. J. *Principles of Polymer Physics*; Cornell University Press: Ithaca, NY, 1981.
(35) Huggins, M. L. Some properties of solutions of long-chain compounds. *J. Phys. Chem.* **1942**, *46*, 151−158.
(36) Benmouna, M.; Seils, J.; Meier, G.; Patkowski, A.; Fischer, E. W. Critical fluctuations in ternary polymer solutions. *Macromolecules* **1993**, *26*, 668−678.
(37) de Gennes, P.-G. *Scaling Concepts in Polymer Physics*, 1st ed.; Cornell University Press: London, 1979.
(38) Hong, K.; Noolandi, J. Theory of inhomogeneous multicomponent polymer systems. *Macromolecules* **1981**, *14*, 727−736.
(39) Hong, K.; Noolandi, J. Theory of interfacial tension in ternary homopolymer-solvent systems. *Macromolecules* **1981**, *14*, 736−742.
(40) van der Schoot, P. Green-function description of dense polymer systems. *Macromolecules* **2000**, *33*, 8497−8503.
(41) Evans, D. J.; Morriss, P. G.; Craig, D. P.; McWeeny, R. *Statistical Mechanics of Nonequilibrium Liquids*; Academic Press: London, 1990.
(42) Binder, K. Collective diffusion, nucleation, and spinodal decomposition in polymer mixtures. *J. Chem. Phys.* **1983**, *79*, 6387−6409.
(43) Bornside, D. E.; Macosko, W. W.; Scriven, L. E. Spin coating of a PMMA/chlorobenzene solution. *J. Electrochem. Soc.* **1991**, *138*, 317−320.
(44) Cook, H. Brownian motion in spinodal decomposition. *Acta Metall.* **1970**, *18*, 297−306.
(45) Langer, J. S. Theory of spinodal decomposition in alloys. *Ann. Phys.* **1971**, *65*, 53−86.
(46) Hoyt, J. Spinodal decomposition in ternary alloys. *Acta Metall.* **1989**, *37*, 2489−2497.
(47) Hohenberg, P. C.; Halperin, B. I. Theory of dynamic critical phenomena. *Rev. Mod. Phys.* **1977**, *49*, 435−479.
(48) Desai, R. C.; Kapral, R. *Dynamics of Self-Organized and Self-Assembled Structures*; Cambridge University Press: New York, 2009.
(49) Wodo, O.; Ganapathysubramanian, B. Computationally efficient solution to the Cahn-Hilliard equation: Adaptive implicit time schemes, mesh sensitivity analysis and the 3D isoperimetric problem. *J. Comput. Phys.* **2011**, *230*, 6037−6060.
(50) Sariban, A.; Binder, K. Phase separation of polymer mixtures in the presence of solvent. *Macromolecules* **1988**, *21*, 711−726.
(51) Roby, F.; Joanny, J.-F. Dynamics of concentration fluctuations in ternary polymer solutions. *Macromolecules* **1992**, *25*, 4612−4618.
(52) Genz, U. Cooperative diffusion and interdiffusion in polymer solutions. *Macromolecules* **1994**, *27*, 5691−5696.
(53) Vis, M.; Peters, V. F. D.; Erné, B. H.; Tromp, R. H. Ion entropy in phase-separated aqueous mixtures of polyelectrolyte and neutral polymer. *Macromolecules* **2015**, *48*, 2819−2828.
(54) Horst, R. Calculation of phase diagrams not requiring the derivatives of the Gibbs energy demonstrated for a mixture of two homopolymers with the corresponding copolymer. *Macromol. Theory Simul.* **1995**, *4*, 449−458.
(55) Lifshitz, I. M.; Slyozov, V. V. The kinetics of precipitaction from supersaturated solid solutions. *J. Phys. Chem. Solids* **1961**, *19*, 35−50.
(56) Yao, J. H.; Elder, K. R.; Guo, H.; Grant, M. Theory and simulation of Ostwald ripening. *Phys. Rev. B: Condens. Matter Mater. Phys.* **1993**, *47*, 14110−14125.
(57) Petschek, R. G.; Metiu, H. A computer simulation of the time-dependent Ginzburg-Landau model for spinodal decomposition. *J. Chem. Phys.* **1983**, *79*, 3443−3456.

DOI: 10.1021/acs.macromol.6b00537
Macromolecules 2016, 49, 6858−6870